Image Anal Stereol 2026;45: 37-50 doi: 105566/ias.3781
Original Research Paper

IMAGE FUSION FOR ENHANCING DIAGNOSTIC ACCURACY IN MEDICAL IMAGING USING FDCT, HSV, AND DC-PCNN

MUHAMMAD SHAFIQ[1], WAEAL J. OBIDALLAH[2], WANG QUN[1], TAHIR KAMAL[3], ANAS BILAL✉,[4]
[1]School of Computer Science, Shandong Xiehe University, Jinan, China; [2]College of Computer and Information Sciences, Imam Mohammad Ibn Saud Islamic University (IMSIU), Riyadh, 11673, Saudi Arabia; [3]3School of Information and Software Engineering, University of Electronic Science and Technology of China, Chengdu, China; [3]College of Information Science & Technology, Hainan Normal University, Haikou, China.
e-mail: shafiqk786@hotmail.com, wobaidallah@imamu.edu.sa, wangqun@sdxiehe.edu.cn, tahirkamal2@uestc.edu.cn, a.bilal19@yahoo.com
(Received October 10, 2025; revised February 9, 2026; accepted February 19, 2026)

ABSTRACT

Image-based disease diagnosis and treatment have long been used to enhance human health and well-being. Recent advancements in imaging and image processing technologies have spurred significant research in this field, leading to improvement in image modalities that allow better representation of features, ultimately helping healthcare practitioners make more precise diagnoses and treatment plans. Various medical image modalities, including X-rays, Positron Emission Tomography (PET), Computer Tomography (CT), and Magnetic Resonance Imaging (MRI), are widely used. Each modality has its strengths; for instance, MRI provides detailed anatomical information, while PET reveals functional and metabolic data. However, using these modalities separately limits diagnostic potential, as they cannot provide a comprehensive view of both structure and function. The Image Fusion Model (IFM) is designed to overcome this limitation by combining features from both images. Existing IFMs often face challenges such as the loss of high-frequency details, insufficient retention of structural data, and poor preservation of functional information. The proposed model integrates the Fast Discrete Cosine Transform (FDCT), the HSV color model, and a Dual-Channel Pulse-Coupled Neural Network (DC-PCNN) to address these challenges. The model was evaluated using eight MRI and PET image pairs from the Harvard Medical School Image Database, demonstrating competitive performance in terms of spatial frequency (SF), mutual information (MI), image entropy (IE), image quality index (IQI), and margin information retention (MIR). The results show that the proposed model outperforms traditional methods, particularly in preserving high-frequency details while maintaining both structural and functional data integrity.

Keywords: diagnostic imaging, Dual-Channel Pulse-Coupled Neural Network, FDCT, HSV color model, image fusion model, image processing, medical image fusion, medical imaging, MRI.

INTRODUCTION

Medical imaging is a non-invasive method that has long been used by medical professionals to visualize and diagnose various diseases (Abhisheka *et al.*, 2024, Islam *et al.*, 2023). Recently, many improvements have been completed in the field of imaging and image processing that enhanced the various image modalities (Abhisheka *et al.*, 2023, Bilal *et al.*, 2024a, Haribabu *et al.*, 2023). Among the most commonly used imaging modalities are Magnetic Resonance Imaging (MRI) and Positron Emission Tomography (PET) (Furtado *et al.*, 2023). The MRI uses a large magnet, radio waves, and a computer to generate anatomical details of the body's internal organs (Bilal *et al.*, 2024b, Murtaza *et al.*, 2020). PET uses a safe chemical called a radiotracer that is injected into the body, and a device called a PET scanner generates images of internal organs and tissues (Arabi *et al.*, 2024). Each modality has its unique way of representing the details of the organs.

The MRI provides high-resolution structural information, while PET provides the functional information of the organs (Perez *et al.*, 2023). However, using these modalities separately limits their diagnostic potential, as they cannot propose a comprehensive view of structure and function (Bilal *et al.*, 2024c). Fusing the modalities and providing them as one comprehensive image will give more information and features for medical experts to make more accurate diagnoses and provide precise treatment based on the improved image fusion (Bilal *et al.*, 2023). The goal of the Image Fusion Model (IFM), particularly in medical imaging, is to create a combined

image that enhances human visual perception (Singh *et al.*, 2023). A more standard approach in image fusion accepts the mean of input images, reducing feature dissimilarity (Karim *et al.*, 2023). Laplacian pyramid-based image fusion is used to overcome this limitation, but it introduces its own set of drawbacks, such as blocking artifacts (Singh and Bhandari, 2024).

The earliest model proposed to fuse MRI and PET employed (Li *et al.*, 1995) wavelet transform, and the area-based maximum selection rule was used for the coefficient selection and activity measures to fuse the two images. A recent attempt (Preethi and Aishwarya, 2021) to fuse MRI and PET was done using the Discrete Wavelet Transform (DWT) and Spider Monkey Optimization (SMO) algorithm. To handle the limited directionalities constraint of DWT, the researchers (Ashwanth and Swamy, 2020) had proposed a DWT combined with the Stationary Wavelet Transform (SWT) model to fuse the MRI and PET images. They used edge-based fusion for Low Frequencies (LF) and energy-based fusion for high frequencies. A pixel-based decomposition using Discrete Cosine Transform (DCT) combined with DWT was proposed by (Amiri *et al.*, 2021) to fuse medical images. They performed the fusion in two stages: DCT decomposition and DWT fusion. To maintain the spectral and spatial resolution features of the input images, the work (Nobariyan *et al.*, 2018) used YCbCr to preserve spatial information and Discrete Wavelet Transforms (DWT) to preserve spectral information and proved that their model is better than other models such as YCbCr Brovey, Laplacian-pyramid, Contourlet, and DWT.

However effective, the DWT could not represent the necessary curves and edges of images (Rana and Degadwala, 2014). To overcome these limitations, several transform models was used for fusing MRI and PET. A Non-Subsampled Shearlet Transform Model (NSSTM) combined with a Retina-Inspired Model (RIT) was used (Sayadi *et al.*, 2020) for the MRI and PET fusion. By integrating the Two-Dimensional Hilbert transform (2-D HT) and intensity hue saturation (IHS) method (Haddadpour *et al.*, 2017), we have proposed an IFM. They tried this combination to enhance the spatial and spectral information. Traditional IFMs have often failed to preserve essential structural and functional details simultaneously. As a result, the IFM ensues with limited information, and further such models introduce objects that degrade the quality of the fused image.

Further methods cannot preserve HF features contributing to the image's sharpness and boundary data. To handle these limitations, the Pulse Coupled Neural Network (PCNN) model have been used in various works to fuse multimodal images. The PCNN is a biological-inspired Neural Network (NN) model that was proposed by (Eckhorn *et al.*, 1989), and many improvements have been made to this base model (Johnson and Padgett, 1999, Johnson *et al.*, 1998, Johnson and Ritter, 1993, Ranganath *et al.*, 1995). These advancements have made PCNN a suitable model for image segmentation, image enhancement, pattern recognition, and Image fusion. The original PCNN has one input for each neuron; the invention of the PCNN-based image fusion models is complex as multiple PCNN models are required for fusion. This limitation is overcome by a Dual-Channel Pulse-Coupled Neural Network (DC-PCNN) (Wang and Ma, 2007), which can take multiple inputs for each neuron.

This work presents a hybrid fusion model to overcome the limitations discussed above. The proposed model combines a Fast Discrete Cosine Transform (FDCT), an HSV color model, and a DC-PCNN for MRI and PET image fusion. It is important to note that while the DC-PCNN uses adaptive rules, this is not a machine learning-based approach. Rather, it is a hand-designed, adaptive image processing technique that does not involve training or parameter optimization. The input MRI image is decomposed into High Frequency (HF) and Low Frequency (LF) sub-bands. Simultaneously, the PET image is decomposed into hue, saturation, and value using HSV transform. The V component is further decomposed into HF and LF sub-bands. The HF component from MRI and PET is processed using the DC-PCNN; the work utilizes dynamic threshold and firing rules to fuse the HF component. The LF component is fused by employing a contrast-based weighting approach. The fused image is then reconstructed using inverse HSV and inverse FDCT. The model was evaluated for Spatial Frequency (SF), Mutual Information (MI), Image Entropy (IE), Image Quality Index (IDI) and Margin Information Retention (MIR). Using image modalities from the Harvard Medical School Image Database, the proposed model was compared against other models for the above metrics, which showed that the proposed model had outperformed the other models on several metrics, though some performance was mixed.

The objectives of the work are:

(a) To combine the strengths of Fast Discrete Cosine Transform (FDCT), HSV color model, and DC-PCNN for effective fusion of MRI and PET images.
(b) Utilize dynamic thresholding and firing rules in DC-PCNN to fuse HF components from MRI and PET images.

(c) Apply a contrast-based weighting approach to fuse LF components, improving the fused image's overall contrast and brightness retention.
(d) Reconstruct the fused image using inverse HSV and inverse FDCT.
(e) Assess the proposed model's effectiveness through SF, MI, IE, IQI, and MIR metrics.

The paper is organized as follows: Section 2 deals with the proposed methodology, Section 3 presents the experiment analysis, and Section 4 concludes the work.

METHODOLOGY

The proposed fusion model is presented in Fig. 1, and the following section details the overall process. Fig. 1 indicates that PET images are transformed into H, S, and V components. The FDCT decomposes the MRI image and V components into HF and LF subbands. The HF component is fused using DC-PCNN and the LF component is fused using a contract-based weighting. The fused images are reconstructed using I-HSV and I-FDCT.

Transformation of PET Images Using the HSV Color Model

PET transformation decomposes PET images into dimensions, such as hue, saturation, and value components.

The HSV decomposition steps are as follows:

i. **Determination of Maximum and Minimum RGB Values:** Identify the maximum $(k_{\max})$ and minimum $(k_{\min})$ values across the RGB components of each pixel. This range is critical for calculating Eq. (1)' s saturation and value components.

$$k = k_{\max} - k_{\min} \tag{1}$$

ii. **Calculation of Saturation (S):** Saturation reflects the depth of color and indicates the concentration of radiotracer uptake, an essential aspect in PET imaging diagnostics.

It is computed as follows: Eq. (2).

$$S = \begin{cases} 0 & \text{If } k_{\max} = 0, \\ & \text{Indicating a lack of color differentiation} \\ \frac{k}{k_{\max}} & \text{Otherwise} \end{cases} \tag{2}$$

iii. **Calculation of Value (V):** The value component, representing the pixel's intensity, correlates directly with the tracer activity levels in PET scans.

It is clear as Eq. (3),

$$V = k_{\max} \tag{3}$$

iv. **Derivation of Hue (H):** Hue quantifies the color type and is particularly useful for differentiating functional responses in tissues.

It is determined by the dominant RGB component and is measured by Eq. (4).

$$H = \begin{cases} 60^\circ \times \frac{G-B}{k} \bmod 360^\circ & \text{if } k_{\max} = R \\ 60^\circ \times \left(2 + \frac{B-R}{k}\right) \bmod 360^\circ & \text{if } k_{\max} = G \\ 60^\circ \times \left(4 + \frac{R-G}{k}\right) \bmod 360^\circ & \text{if } k_{\max} = B \end{cases} \tag{4}$$

The procedure of converting HSV back to RGB depends on the hue sector (which of the 6 elements of the hue wheel the color lies within).

Here's a breakdown of the transformations:

1 **Calculate RGB from HSV**: Identify which sector of the hue circle the hue value H falls into. Hue H is typically expressed in degrees, ranging from 0 to 360 degrees.

2 **Calculate Chroma (C)**: Chroma, which represents the saturation of the color, is given by Eq. (5).

$$C = V \times S \tag{5}$$

where V (value) is the maximum RGB value and S (saturation) measures color intensity relative to brightness.

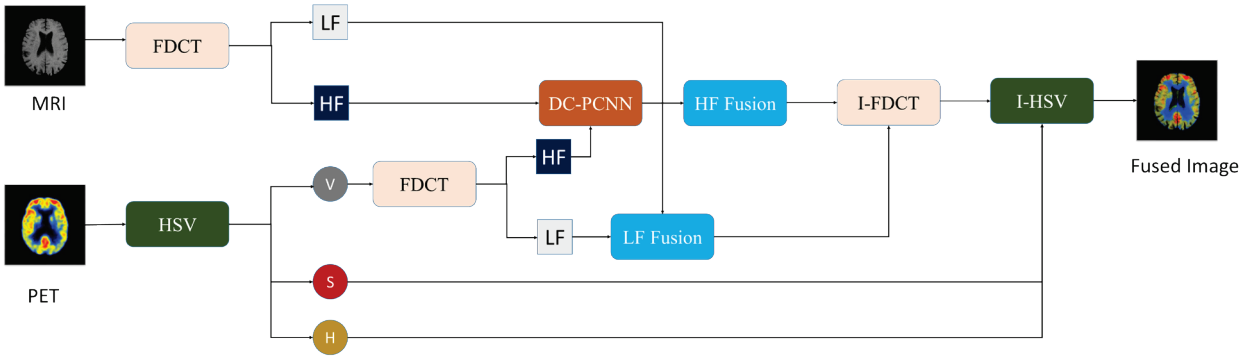

Fig. 1. *Proposed fusion model.*

3 Calculate X and:

- X is the second-largest component of the color and is defined as Eq. (6).

$$X = C \times \left(1 - \left|\frac{H}{60^\circ}\text{MOD}2 - 1\right|\right) \quad (6)$$

- m is calculated to match the lightness of the color, Eq. (7).

$$m = V - C \quad (7)$$

4 Determine RGB Values: Depending on which sector H falls into, RGB values are adjusted accordingly Eq. (8).

$$(R,G,B) = \begin{cases} (C+m, X+m, m) & \text{if } 0^\circ \le H < 60^\circ \\ (X+m, C+m, m) & \text{if } 60^\circ \le H < 120^\circ \\ (m, C+m, X+m) & \text{if } 120^\circ \le H < 180^\circ \\ (m, X+m, C+m) & \text{if } 180^\circ \le H < 240^\circ \\ (X+m, m, C+m) & \text{if } 240^\circ \le H < 300^\circ \\ (C+m, m, X+m) & \text{if } 300^\circ \le H < 360^\circ \end{cases} \quad (8)$$

Adjusted these values to ensure they are within the range [0,1] if working with normalized values or [0,255] for standard 8-bit images.

Fast Discrete Cosine Transform (FDCT) for MRI Images

The FDCT decomposes the input image into HF and LF components. Initially, the input image is separated into non-overlapping blocks of size $N \times N$ (e.g., 8×8 or 16×16 pixels). The FDCT then transforms a block of image pixels from the spatial domain into the frequency domain, Eq. (9).

$$F(u,v) = \frac{1}{4} C(u)\, C(v) \sum_{m=0}^{N-1} \sum_{n=0}^{N-1} f(x,y) \cos\left[\frac{(2m+1)u\pi}{2N}\right] \cos\left[\frac{(2n+1)v\pi}{2N}\right] \quad (9)$$

where $F(u,v)$ represents the DCT coefficient at frequencies u and v, $f(m,n)$ indicates the pixel intensity at coordinates m and n, and $C(u)$ and $C(v)$ are normalization factors, defined as Eq. (10).

$$C(w) = \begin{cases} \frac{1}{\sqrt{2}} & \text{if } w = 0 \\ 1 & \text{otherwise} \end{cases} \quad (10)$$

After applying FDCT, the transformed coefficients $F(u,v)$ are analyzed to separate HF and LF components. The LF components, located at the top-left corner of the DCT block, encapsulate a significant share of the signal energy, which includes basic shapes and smooth variations in the image. Conversely, HF components in the bottom-right corner represent edges and fine details.

A threshold is defined as Eq. (11) and Eq. (12) to extract the LF and HF components.

$$LF(u,v) = \begin{cases} F(u,v) & \text{for } u,v \le \text{threshold} \\ 0 & \text{otherwise} \end{cases} \quad (11)$$

$$HF(u,v) = \begin{cases} F(u,v) & \text{for } u,v > \text{threshold} \\ 0 & \text{otherwise} \end{cases} \quad (12)$$

The Eq. (13) for reconstructing the LF component from its DCT coefficients is given by:

$$f_{LF}(m,n) = \frac{1}{4} \sum_{u=0}^{T} \sum_{v=0}^{T} C(u)\, C(v) F(u,v) \cos\left[\frac{(2m+1)u\pi}{2N}\right] \cos\left[\frac{(2n+1)v\pi}{2N}\right] \quad (13)$$

The reconstruction of the HF component is described by Eq. (14).

$$f_{HF}(m,n) = \frac{1}{4} \sum_{u,v>T}^{N-1} C(u)\, C(v)\, F(u,v) \cos\left[\frac{(2m+1)u\pi}{2N}\right] \cos\left[\frac{(2n+1)v\pi}{2N}\right] \quad (14)$$

In this configuration, $u, v > T$ indicates that the sums are taken over the frequencies from just above the threshold T to $N-1$, thus isolating and enhancing the HF details. To reconstruct the spatial domain representation from these frequency components, inverse FDCT (IDCT) is applied to both HF and LF blocks.

The IDCT formula is Eq. (15).

$$f'(m,n) = \frac{1}{4} \sum_{u=0}^{N-1} \sum_{v=0}^{N-1} C(u) C(v) F(u,v) \cos\left[\frac{(2m+1)u\pi}{2N}\right] \cos\left[\frac{(2n+1)v\pi}{2N}\right] \quad (15)$$

where $f'(m,n)$ represents the reconstructed pixel value at coordinates $(m,n$. This method allows for significant enhancement and detailed analysis of MRI images, aiding in more precise medical diagnostics.

DC-PCNN Neural Network Structure

Let $I_{HF}(m,n)$ represent the HF intensity value of the pixel at coordinates (m,n) in the image, where $I_{HF}^{MRI}(m,n)$ and $I_{HF}^{PET}(m,n)$) denote the HF components from MRI and PET images, respectively. Correspondingly, the neuron located at the exact coordinates in the DC-PCNN will directly process these intensity values. Each neuron in the DC-PCNN comprises several components (Fig. 2) that simulate the biological processing of visual stimuli. The external stimulus $F(m,n,t)$ for each neuron is calculated based on the HF intensity

values $I_{HF}^{MRI}(m,n)$ and $I_{HF}^{PET}(m,n)$. DC-PCNN is an adaptive image processing technique and not a machine learning-based model. No data training or optimization is involved. The neuron outputs are based on dynamic thresholds and rules.

The stimulus reflects the influence of the HF features from both modalities, Eq. (16) and Eq. (17).

$$F_{HF}^{MRI}(m,n,t) = I_{HF}^{MRI}(m,n) + \alpha_{MRI}\sum_{i,j} W_{ij}^{MRI}\, Y_{MRI}(i,j,t-1) \quad (16)$$

$$F_{HF}^{PET}(m,n,t) = I_{HF}^{PET}(m,n) + \alpha_{PET}\sum_{i,j} W_{ij}^{PET}\, Y_{PET}(i,j,t-1) \quad (17)$$

Here, α is a scaling factor, and W_{ij} are the weights that determine the influence of neighboring neurons' previous activations. To enhance or suppress features based on the surrounding context, the DC-PCNN employs a Linking Field (L). The linking field $L(m,n,t)$ employs the information from neighboring neurons to enhance or suppress features based on the surrounding context, Eq. (18) and Eq. (19).

$$L_{HF}^{MRI}(m,n,t) = \beta_{MRI}\sum_{i,j} K_{ij}^{MRI}\, Y_{MRI}(i,j,t) \quad (18)$$

$$L_{HF}^{PET}(m,n,t) = \beta_{PET}\sum_{i,j} K_{ij}^{PET}\, Y_{PET}(i,j,t) \quad (19)$$

The parameters β and K_{ij} control the degree and nature of this neighborhood influence. The dynamic threshold $\theta(m,n,t)$ is used to adapt the network over time to regulate neuron firing, such that only significant HF features from MRI and PET images contribute to the fusion process, Eq. (20) and Eq. (21).

$$\theta_{HF}^{MRI}(m,n,t) = e^{-\lambda_{MRI}}\theta_{HF}^{MRI}(m,n,t-1) + \gamma_{MRI}\, Y_{MRI}(m,n,t) \quad (20)$$

$$\theta_{HF}^{PET}(m,n,t) = e^{-\lambda_{PET}}\theta_{HF}^{PET}(m,n,t-1) + \gamma_{PET}\, Y_{PET}(m,n,t) \quad (21)$$

The parameters λ and γ govern the decay and update of the threshold, balancing sensitivity and selectivity in feature detection. The output $Y(m,n,t)$ of each neuron, which represents the processed HF information, is determined by the external stimulus, linking field, and dynamic threshold, Eq. (22) and Eq. (23).

$$Y_{HF}^{MRI}(m,n,t) = f\left(F_{HF}^{MRI}(m,n,t), L_{HF}^{MRI}(m,n,t), \theta_{HF}^{MRI}(m,n,t)\right) \quad (22)$$

$$Y_{HF}^{PET}(m,n,t) = f\left(F_{HF}^{PET}(m,n,t), L_{HF}^{PET}(m,n,t), \theta_{HF}^{PET}(m,n,t)\right) \quad (23)$$

The function $f(\cdot)$ combines these components, frequently through a non-linear activation function, to produce the final output that will be used in the fusion process. The results from the MRI and PET channels are then fused to generate a combined HF component, Eq. (24).

$$Y_{HF}^{\text{fused}}(m,n) = \eta \cdot Y_{HF}^{MRI}(m,n) + (1-\eta) \cdot Y_{HF}^{PET}(m,n) \quad (24)$$

Here, η is a weighting factor that controls the contribution of each modality to the final fused HF image.

Adaptive Synaptic Weights

In the DC-PCNN, the synaptic weights W_{ij} between neurons are dynamically updated during the image fusion process. These weights represent the combined influence of the local neuron and its neighboring neurons at a location (x,y). The adaptive update of these synaptic weights is based on the neuron's output at the previous time step and the features of both the local pixel and its neighbors as expressed as Eq. (25).

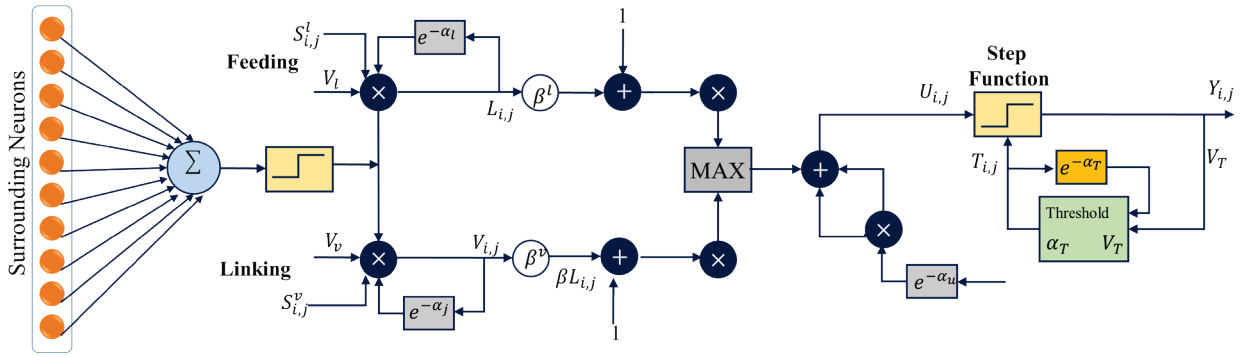

Fig. 2. *DC-PCNN neuron architecture.*

$$W_{ij}^{MRI}(m,n,t) = W_{ij}^{MRI}(m,n,t-1) + \delta_{MRI} \cdot \left(Y_{MRI}(i,j,t-1) + \sum_{p,q} \psi_{pq}^{MRI}(m,n) Y_{MRI}(p,q,t-1)\right) \quad (25)$$

Similarly, for the PET channel, Eq. (26).

$$W_{ij}^{PET}(m,n,t) = W_{ij}^{PET}(m,n,t-1) + \delta_{PET} \cdot \left(\left(Y_{PET}(i,j,t-1) + \sum_{p,q} \psi_{pq}^{PET}(m,n) Y_{PET}(p,q,t-1)\right)\right) \quad (26)$$

Here, δ_{MRI} and δ_{PET} are learning rates that control the degree of weight adaptation while $\psi_{pq}^{MRI}(m,n)$ and $\psi_{pq}^{PET}(m,n)$ represent the influence of neighboring pixels (p,q) on the current neuron's weight adaptation. The updated synaptic weights are then used to modulate both the external stimulus $F(m,n,t)$ and the linking field $L(m,n,t)$, which together determine the neuron's output which is given by Eq. (27).

$$F_{HF}^{MRI}(m,n,t) = I_{HF}^{MRI}(m,n) + \alpha_{MRI} \sum_{i,j} W_{ij}^{MRI}(m,n,t) Y_{MRI}(i,j,t-1) \quad (27)$$

For the PET channel, the corresponding stimulus is Eq. (28).

$$F_{HF}^{PET}(m,n,t) = I_{HF}^{PET}(m,n) + \alpha_{PET} \sum_{i,j} W_{ij}^{PET}(m,n,t) Y_{PET}(i,j,t-1) \quad (28)$$

Similarly, the linking field, which aggregates the influence of surrounding neurons, is adjusted using the newly updated synaptic weights Eq. (29) and Eq. (30).

$$L_{HF}^{MRI}(m,n,t) = \beta_{MRI} \sum_{i,j} K_{ij}^{MRI} W_{ij}^{MRI}(m,n,t) Y_{MRI}(i,j,t) \quad (29)$$

$$L_{HF}^{PET}(m,n,t) = \beta_{PET} \sum_{i,j} K_{ij}^{PET} W_{ij}^{PET}(m,n,t) Y_{PET}(i,j,t) \quad (30)$$

Adaptive Link Strength

The linking strength for each channel is denoted as $\beta_{ij,MRI}^{HF}(t)$ and $\beta_{ij,PET}^{HF}(t)$, for the MRI and PET-HF components, respectively. The linking strength is dynamically adjusted based on local HF features around each neuron $'i', EQ(31)$ *and* $EQU(32)$.

$$\beta_{ij,MRI}^{HF}(t) = \kappa_{MRI}\left(\mathrm{HF}_{ij,MRI}\right) \quad (31)$$

$$\beta_{ij,PET}^{HF}(t) = \kappa_{PET}\left(\mathrm{HF}_{ij,PET}\right) \quad (32)$$

where, κ_{MRI} and κ_{PET} are functions that adjust the linking strength based on the HF features specific to each modality, such as edge sharpness in MRI and texture contrast in PET, Eq. (33).

$$\kappa_{MRI}\left(E_{ij,MRI}\right) = \lambda_{\beta,MRI} \cdot \mathrm{Norm}\left(E_{ij,MRI}\right) \quad (33)$$

where, $\lambda_{\beta,MRI}$ is edge scaling factor, and $\mathrm{Norm}\left(E_{ij,MRI}\right)$ is a normalization function that standardizes the edge strength values across the MRI image, Eq. (34).

$$\kappa_{PET}\left(T_{ij,PET}\right) = \xi_{\beta,PET} \cdot \mathrm{Norm}\left(T_{ij,PET}\right) \quad (34)$$

Where $\xi_{\beta,PET}$ is texture contrast scaling factor, and $\mathrm{Norm}\left(T_{ij,PET}\right)$ normalizes the texture contrast values in the PET image.

Dynamic Threshold

The threshold for neuron i in each channel, denoted as $\theta_{i,MRI}^{HF}(t)$ for MRI and $\theta_{i,PET}^{HF}(t)$ for PET, is updated over time based on its past value and the neuron's firing history, Eq. (35) and Eq. (36).

$$\theta_{i,MRI}^{HF}(t) = \theta_{i,MRI}^{HF}(t-1) \cdot e^{-\lambda_{\theta,MRI}} + \gamma_{\theta,MRI} \cdot Y_{i,MRI}^{HF}(t-1) \quad (35)$$

$$\theta_{i,PET}^{HF}(t) = \theta_{i,PET}^{HF}(t-1) \cdot e^{-\lambda_{\theta,PET}} + \gamma_{\theta,PET} \cdot Y_{i,PET}^{HF}(t-1) \quad (36)$$

Where, $\lambda_{\theta,MRI}$ and $\lambda_{\theta,PET}$ are the threshold decay constants for MRI and PET, respectively, $\gamma_{\theta,MRI}$ and $\gamma_{\theta,PET}$ are the contributions to the threshold from the last neuron firing in the MRI and PET channels, respectively, $Y_{i,MRI}^{HF}(t-1)$ and $Y_{i,PET}^{HF}(t-1)$ are the neuron outputs at the previous time step for MRI and PET.

The Edge Strength in MRI is presented as Eq. (37).

$$\theta_{i,MRI}^{HF}(t) = \theta_{i,MRI}^{HF}(t-1) \cdot e^{-\lambda_{\theta,MRI}(E_{i,MRI})} + \gamma_{\theta,MRI}\left(E_{i,MRI}\right) \cdot Y_{i,MRI}^{HF}(t-1) \quad (37)$$

where, $E_{i,MRI}$ represents the edge strength at neuron $'i'$, and $\lambda_{\theta,MRI}\left(E_{i,MRI}\right), \gamma_{\theta,MRI}\left(E_{i,MRI}\right)$ are functions are decay constant and contribution value based on the HF edge information in the MRI channel.

The Texture Contrast in PET is presented as Eq. (38).

$$\theta_{i,PET}^{HF}(t) = \theta_{i,PET}^{HF}(t-1) \cdot e^{-\lambda_{\theta,PET}(T_{i,PET})} + \gamma_{\theta,PET}\left(T_{i,PET}\right) \cdot Y_{i,PET}^{HF}(t-1) \quad (38)$$

Here, $T_{i,PET}$ represents the texture contrast at neuron i in the PET image, with $\lambda_{\theta,PET}\left(T_{i,PET}\right)$ and $\gamma_{\theta,PET}\left(T_{i,PET}\right)$ adjusting the threshold dynamics, based on the HF texture information in the PET channel.

Fusion Rule

Fusion Rule

The fusion of HF components from MRI and PET images uses a dynamic threshold to enhance critical features selectively. Each neuron's input stimulus $F_{i,j}^{\text{mod}}(t)$, from the HF components of MRI (or) PET is compared against the dynamic threshold $\theta_{i,j}^{\text{mod}}(t)$

The neuron fires if the stimulus exceeds this threshold, Eq. (39).

$$Y_{i,j}^{\text{MOD}}(t) = \begin{cases} 1 & \text{If } F_{i,j}^{\text{MOD}}(t) > \theta_{i,j}^{\text{MOD}}(t) \\ 0 & \text{Otherwise} \end{cases} \quad (39)$$

The Threshold $\theta_{i,j}^{\text{mod}}(t)$ dynamically adjusts over time, decreasing unless the neuron fires, which increases the threshold based on recent activity, Eq. (40).

$$\theta_{i,j}^{\text{mod}}(t) = \theta_{i,j}^{\text{mod}}(t-1) \cdot e^{-\lambda} + \gamma \cdot Y_{i,j}^{\text{mod}}(t-1) \quad (40)$$

The fused HF component combines the features from MRI and PET based on neuron activations, Eq. (41).

$$I_{HF}^{\text{fused}}(m,n) = \max\left(Y_{m,\text{n}}^{MRI}(t) \cdot I_{HF}^{MRI}(m,n), Y_{m,n}^{PET}(t) \cdot I_{HF}^{PET}(m,n)\right) \quad (41)$$

This rule ensures that the final IFM uses only the most prominent features from both modalities.

LF Fusion Rule

The LF fusion rule combines the LF components from MRI and PET using a weighted average, Eq. (42).

$$I_{LF}^{\text{fused}}(m,n) = \alpha \cdot I_{LF}^{MRI}(m,n) + (1-\alpha) \cdot I_{LF}^{PET}(m,n) \quad (42)$$

Here, α is the weighting factor calculated using the contrast of the LF components from both modalities. The weighting factor $'\alpha'$ is calculated by comparing the contrast of the LF components from MRI and PET.

The contrast for each modality is computed as Eq. (43).

$$\text{Contrast}\left(I_{LF}^{\text{mod}}\right) = \frac{1}{N}\sum_{m=0}^{N-1}\sum_{n=0}^{N-1}\left(I_{LF}^{\text{mod}}(m,n) - \mu_{LF}^{\text{mod}}\right)^2 \quad (43)$$

where, $I_{LF}^{\text{mod}}(m,n)$ is the LF component from MRI or PET, μ_{LF}^{mod} is the mean intensity of the LF component, N is the total number of pixels.

The contrast-based weighting factor α is then determined as Eq. (44).

$$\alpha = \frac{\text{Contrast}\left(I_{LF}^{MRI}\right)}{\text{Contrast}\left(I_{LF}^{MRI}\right) + \text{Contrast}\left(I_{LF}^{PET}\right)} \quad (44)$$

Algorithm: Image Fusion Model Using FDCT, HSV, and DC-PCNN

Input:

- MRI Image
- PET Image

Output:

- Fused Image

1 MRI Decomposition using FDCT

- Divide the MRI image into non-overlapping $N \times N$ blocks.
- Apply FDCT to each block of the MRI image to decompose it into:
- HF Component: I_{HF}^{MRI}
- LF Component: I_{LF}^{MRI}

2 PET Decomposition using HSV and FDCT

- Convert the PET image from RGB to the HSV color space.
- Extract the Hue (H), Saturation (S), and Value (V) components Eq. (45).

$$I_H^{PET}, I_S^{PET}, I_V^{PET} \quad (45)$$

- Apply FDCT to the V (Value) component:
- HF Component: I_{HF}^{PET}
- LF Component: I_{LF}^{PET}

3 HF Fusion using DC-PCNN

- **For Each** pixel at position (x, y):
- **Initialize** the DC-PCNN for both MRI and PET HF components.
- **Input Stimulus Calculation**: Calculate the stimulus $F_{i,j}^{\text{mod}}(t)$ for both MRI and PET using their HF components.
- **Neuron Firing**: Determine the neuron firing based on the dynamic threshold Eq. (46).

$$\theta_{i,j}^{\text{mod}}(t), Y_{i,j}^{\text{MOD}}(t) = \begin{cases} 1 & \text{If } F_{i,j}^{\text{MOD}}(t) > \theta_{i,j}^{\text{MOD}}(t) \\ 0 & \text{Otherwise} \end{cases} \quad (46)$$

- Fuse the HF components based on neuron activation Eq. (47).

$$I_{HF}^{\text{fused}}(x,y) = \max\left(Y_{m,n}^{MRI}(t) \cdot I_{HF}^{MRI}(m,n), Y_{m,n}^{PET}(t) \cdot I_{HF}^{PET}(m,n)\right) \quad (47)$$

4 LF Fusion Using Contrast-Based Weighted Average

- Compute the contrast of the LF components from MRI and PET, Eq. (48).

$$\text{Contrast}\left(I_{LF}^{\text{mod}}\right) = \frac{1}{N}\sum_{m=0}^{N-1}\sum_{n=0}^{N-1}\left(I_{LF}^{\text{mod}}(m,n) - \mu_{LF}^{\text{mod}}\right)^2 \quad (48)$$

- Calculate the weighting factor α, Eq. (49).

$$\alpha = \frac{\text{Contrast}\left(I_{LF}^{MRI}\right)}{\text{Contrast}\left(I_{LF}^{MRI}\right) + \text{Contrast}\left(I_{LF}^{PET}\right)} \quad (49)$$

- Fuse the LF components using the weighted average, Eq. (50).

$$I_{LF}^{\text{fused}}(m,n) = \alpha \cdot I_{LF}^{MRI}(m,n) + (1-\alpha) \cdot I_{LF}^{PET}(m,n) \quad (50)$$

5 Image Reconstruction using I-FDCT

- Apply Inverse FDCT (I-FDCT) to the fused HF and LF components to reconstruct the image Eq. (51).

$$I_{FDCT}^{\text{fused}}(m,n) = \text{I} - \text{FDCT}\left(I_{HF}^{\text{fused}}, I_{LF}^{\text{fused}}\right) \quad (51)$$

6 Inverse HSV Conversion

- Combine the H and S components from the PET image with the fused intensity Eq. (52).

$$I_{FDCT}^{\text{fused}}(m,n) \quad (52)$$

- Apply Inverse HSV (I-HSV) to convert the image to the RGB color space Eq. (53).

$$I_{RGB}^{\text{fused}} = \text{I} - \text{HSV}\left(I_H^{PET}, I_S^{PET}, I_{FDCT}^{\text{fused}}\right) \quad (53)$$

7 Output the Fused Image

- The final fused image I_{RGB}^{fused} combines the anatomical details from MRI and the functional information from PET.

EXPERIMENT ANALYSIS

The experiments were conducted on a system with an Intel Xeon Gold 6258R processor (28 cores, 2.70 GHz), an NVIDIA Tesla V100 GPU (16 GB VRAM), 256 GB of DDR4 RAM, and 2 TB NVMe SSD storage, running on Ubuntu 20.04 LTS. Python 3.9 was used for programming with libraries including OpenCV, NumPy, TensorFlow 2.6, SciPy, and Matplotlib. The MRI and PET images in the image fusion model were sourced from the Harward Medical School Image Database.

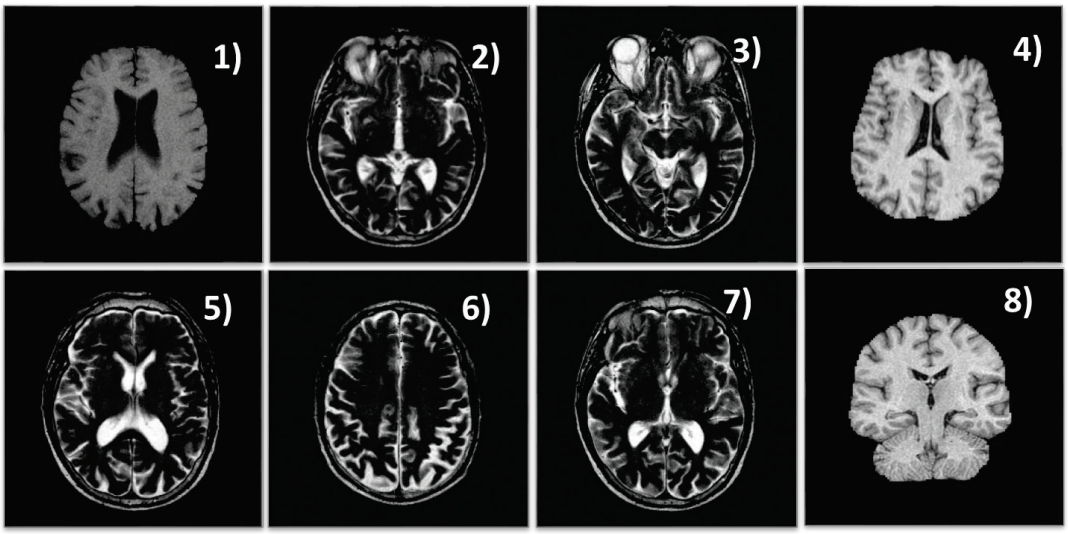

a) MRI

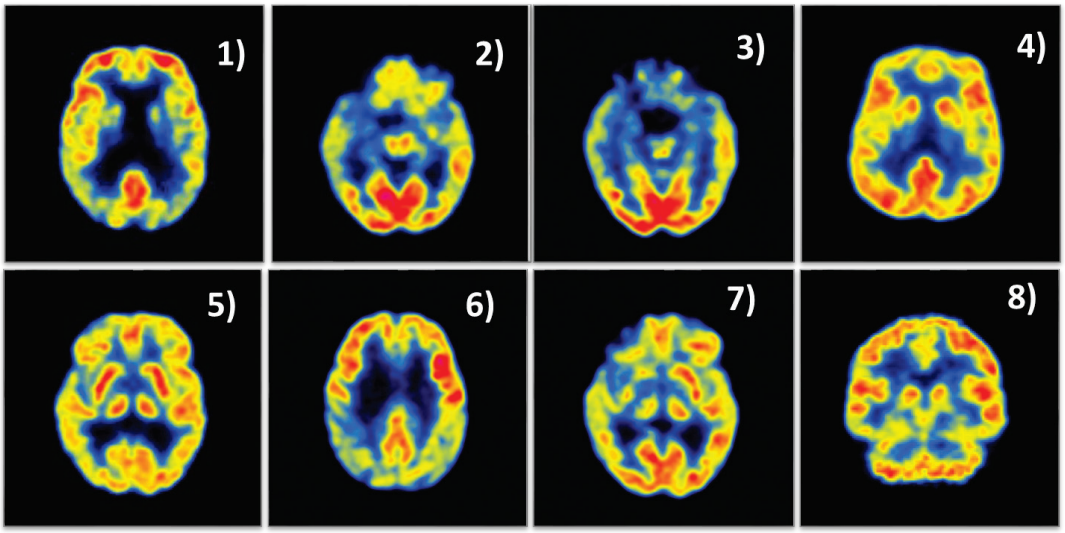

b) PET

Fig. 3. *Images from the Harvard Medical School Image Database were used for the experiment.*

The dataset included MRI and PET images, as shown in Fig. 3a and 3b. As preprocessing, both the images are resized to 256×256 pixels. Intensity normalization was then applied to the images to standardize the pixel intensity values to a range of [0, 1]. A Gaussian filter was then applied to reduce the image noise before fusion.

Using the above images, the fusion performance of the proposed model is compared with other models such as YCbCr-DWT (Nobariyan *et al.*, 2018), 2-D Hilbert – HIS (Haddadpour *et al.*, 2017), HIS-log Gabor (Chen, 2017) and Shearlet (Sayadi *et al.*, 2020) against the metrics such as spatial frequency (SF), mutual information (MI), Image entropy (IE), Image Quality Index (IQI) and Margin Information Retention (MIR) (Q^(AB/F)). The results are discussed in the following sections. Fig. 4 to 8 show the fusion results of the compared models.

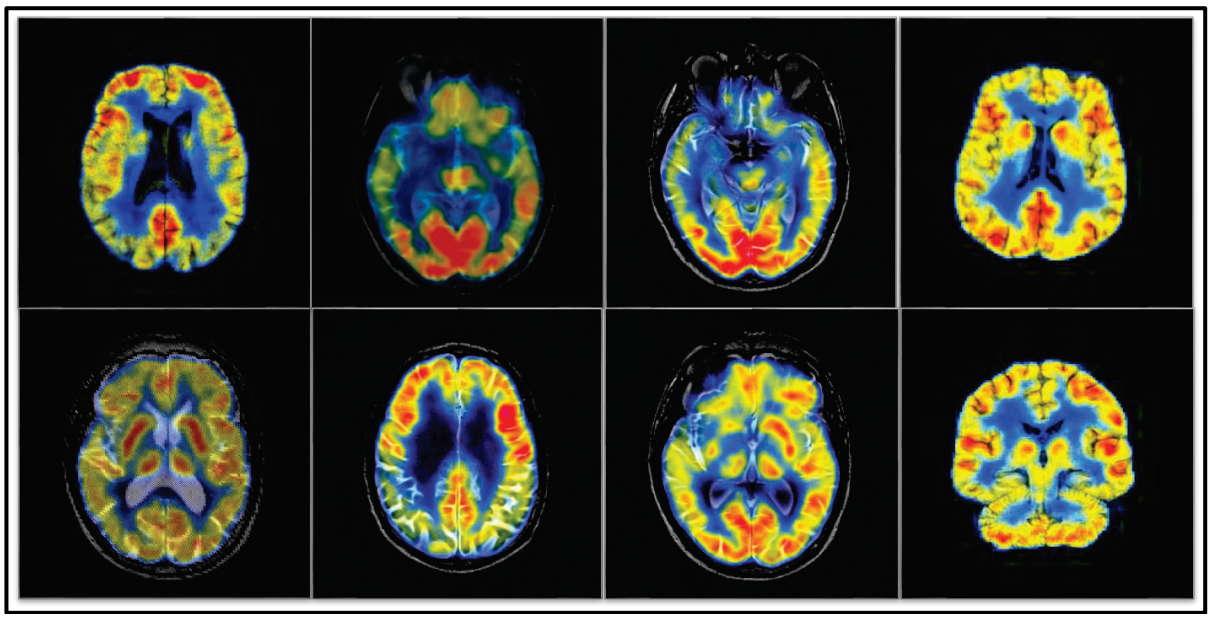

Fig. 4. *YCbCr-DWT fused images.*

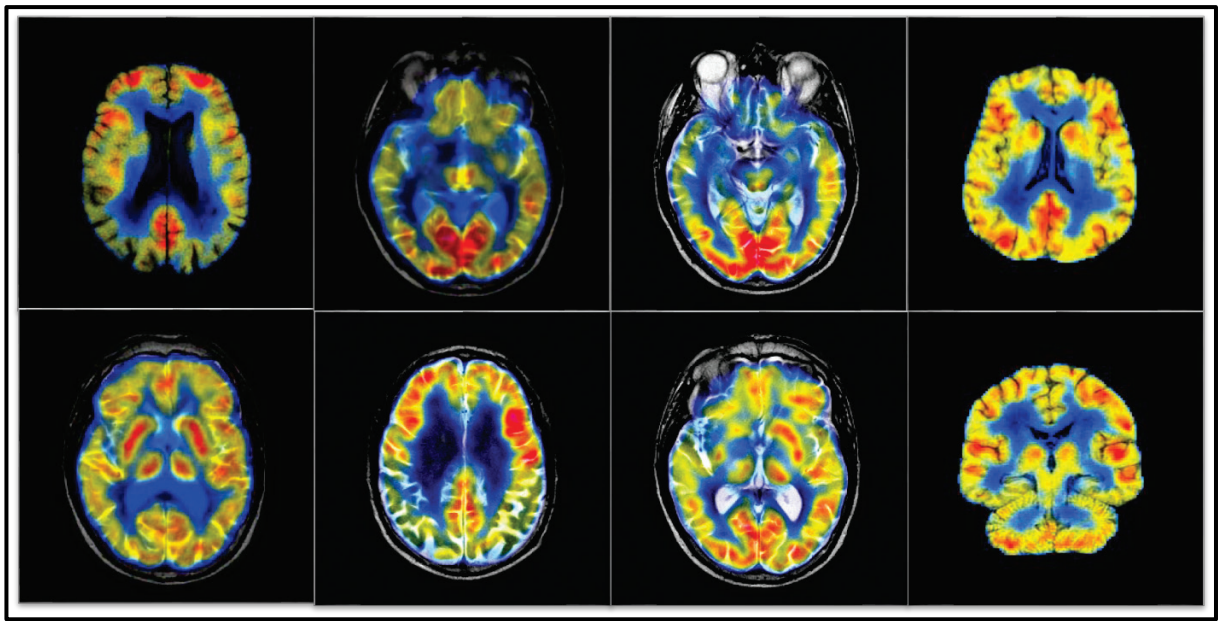

Fig. 5. *2-D Hilbert – HIS fused images.*

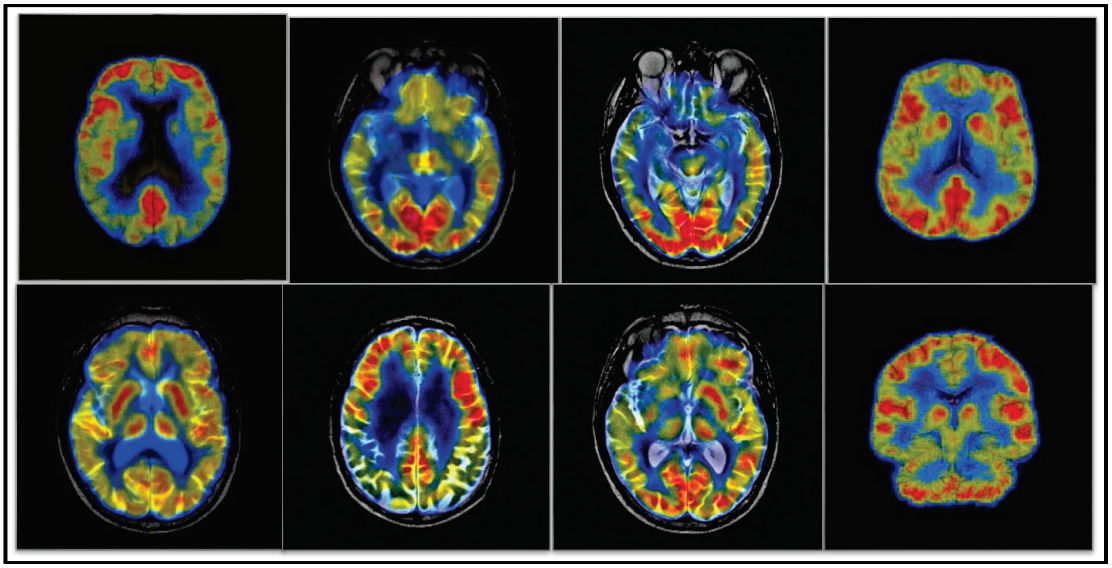

Fig. 6. *HIS-log Gabor Fused images.*

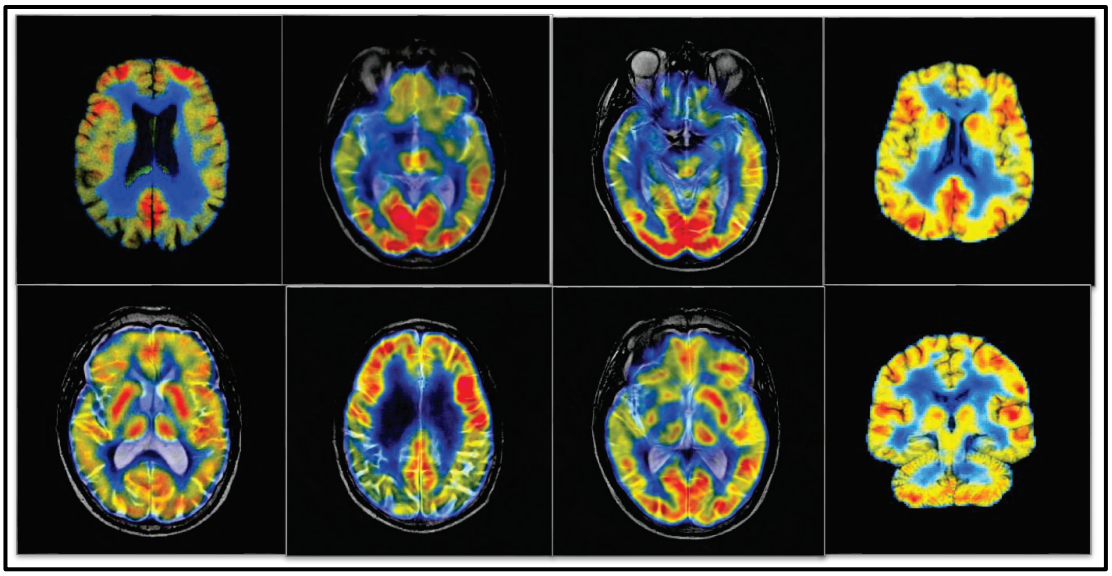

Fig. 7. *Shearlet Fused images.*

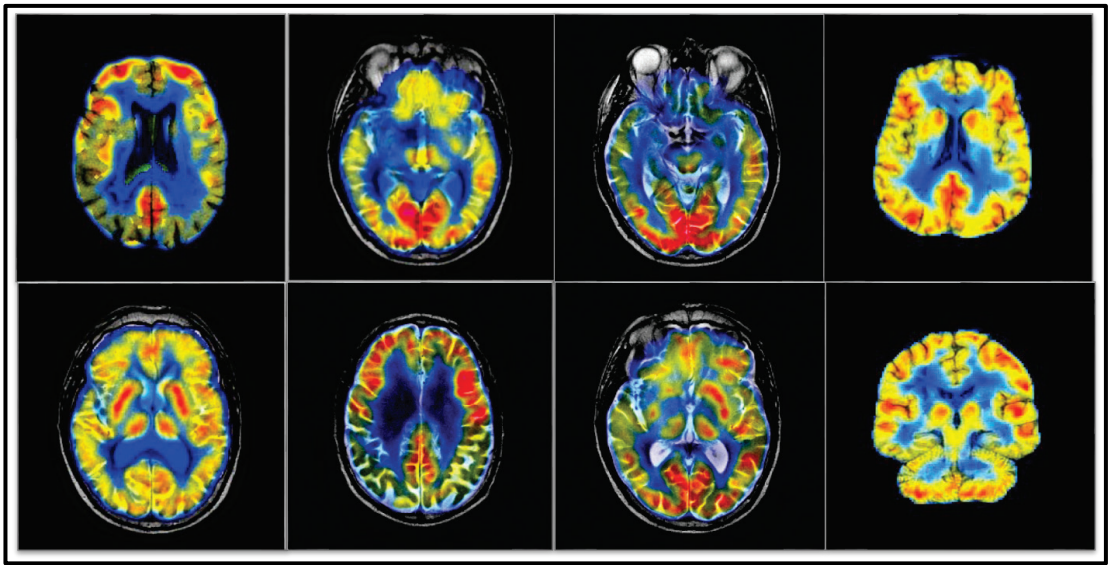

Fig. 8. *Proposed FDCT-HVS-DC PCNN fused images.*

Spatial Frequency (SF) Analysis

The spatial frequency (SF) comparison for the compared models is shown in Fig. 9. The proposed model demonstrates competitive performance compared to the other models. In Img_Set 1, the proposed model achieves an SF value of 31.85, which is higher than Shearlet (28.19) and HIS-log Gabor (24.79), though slightly lower than YCbCr-DWT (33.37). In Img_Set 2, the proposed model scores the highest SF value (38.79), outperforming all other methods. A similar trend is observed in Img_Set 3, where the proposed model achieves the highest SF (32.73), surpassing YCbCr-DWT (26.55) and HIS-log Gabor (26.58). The proposed model also performs well in Img_Set 4, with an SF of 25.86. In Img_Set 5, the proposed model achieves an SF of 32.09, leading over the other methods. In contrast, for Img_Sets 6 and 7, the SF values for the proposed model (20.19 and 17.08, respectively) are competitive but slightly lower than 2-D Hilbert – IHS. Finally, in Img_Set 8, the proposed model records the highest SF value (26.37), much higher than HIS-log Gabor (22.55) and Shearlet (22.02).

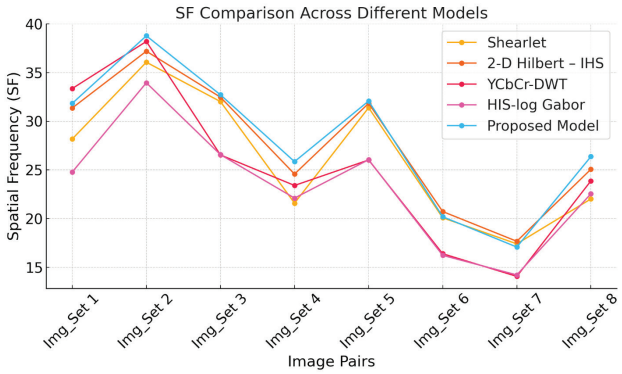

Fig. 9. *Spatial frequency results.*

Image Entropy Analysis

The image entropy (IE) comparison results are shown in Fig. 10. In Img_Set 1, the proposed model records the highest entropy value (4.78) compared to Shearlet and YCbCr-DWT (4.69). Similarly, in Img_Set 2, the proposed model achieves the highest entropy (5.41), outperforming HIS-log Gabor (5.38) and YCbCr-DWT (5.31). The proposed model again leads for Img_Sets 3 and 4, with entropy values of 4.99 and 4.44, respectively. In Img_Set 5, the proposed model records an entropy of 4.95, slightly ahead of HIS-log Gabor (4.91) and YCbCr-DWT (4.83). Notably, in Img_Set 6, the proposed model achieves the highest entropy value (5.56), significantly outperforming all other models. For Img_Set 7, the proposed model (5.30) surpasses 2-D Hilbert – IHS (5.08) and Shearlet (5.11). In Img_Set 8, the proposed model (5.09) again leads over the others.

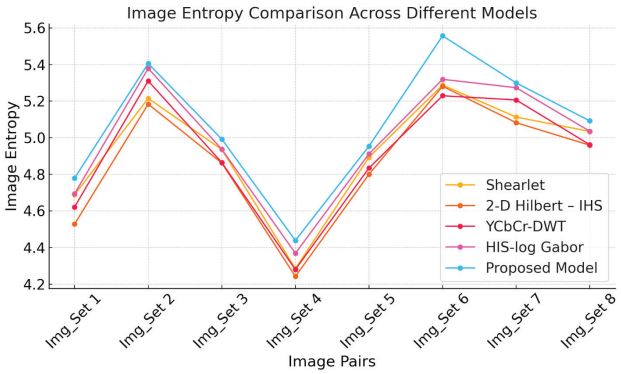

Fig. 10. *IE comparison.*

Mutual Information Analysis

The mutual information (MI) comparison results are shown in Fig. 11. In Img_Set 1, the proposed model achieves the highest MI value (3.08), outperforming YCbCr-DWT (3.02) and HIS-log Gabor (2.79). For Img_Set 2, the proposed model records a substantial MI of 3.68, significantly higher than all other methods, including HIS-log Gabor (2.80) and YCbCr-DWT (2.51). Similar learning is experimental in Img_Set 3, where the proposed model reaches 3.61, outperforming HIS-log Gabor (2.75) and YCbCr-DWT (2.46). In Img_Set 4, the proposed model (2.33) slightly outperforms the others, though the gap is narrower, with HIS-log Gabor following closely at 2.28. For Img_Set 5, the proposed model leads with an MI value of 3.09, surpassing YCbCr-DWT (2.95) and HIS-log Gabor (2.97). The highest MI is observed in Img_Set 6, where the proposed model achieves 3.81, well above HIS-log Gabor (3.51) and other methods. Similarly, in Img_Set 7 (MI = 3.68) and Img_Set 8 (MI = 3.23), the proposed model maintains its dominance against other models.

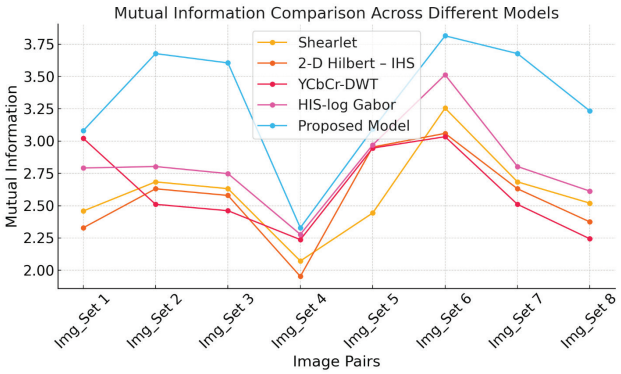

Fig. 11. *MI comparison.*

Image Quality Index Comparison

The assessment of the Image Quality Index (IQI) between the models is shown in Fig. 12. In Img_Set 1, the proposed model records the highest IQI value (0.5021), outperforming HIS-log Gabor (0.4965) and YCbCr-DWT (0.4814). In Img_Set 2, the proposed

model maintains a leading position with an IQI of 0.4930, surpassing YCbCr-DWT (0.4746) and HIS-log Gabor (0.4782). This trend continues in Img_Set 3, where the proposed model (0.4923) outperforms HIS-log Gabor (0.4868) and YCbCr-DWT (0.4720). For Img_Set 4, the proposed model records the highest IQI (0.5092), indicating overall quality compared to other methods. In Img_Set 5, the proposed model again leads with 0.4846, surpassing YCbCr-DWT (0.4699) and HIS-log Gabor (0.4430). The most significant improvement is seen in Img_Set 6, where the proposed model achieves the highest IQI (0.5928), far exceeding YCbCr-DWT (0.5735) and HIS-log Gabor (0.5268). For Img_Set 7, the proposed model performs well with an IQI of 0.4753, outperforming the other methods. Finally, in Img_Set 8, the proposed model (0.4833) achieves the highest IQI among all other models.

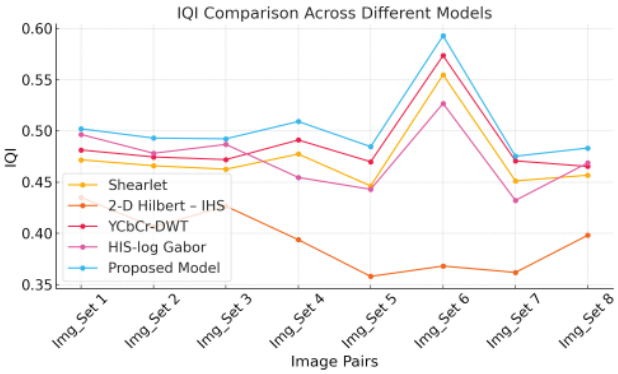

Fig. 12. *IQI comparison.*

$Q^{AB/F}$ Comparison

The MRI comparison results are shown in Fig. 13. In Img_Set 1, the proposed model achieves the highest Q^(AB/F) value (0.5432), surpassing HIS-log Gabor (0.5199) and all other methods. In Img_Set 2, the proposed model achieves a significantly higher value (0.6781) compared to YCbCr-DWT (0.6207) and HIS-log Gabor (0.6008). Similarly, in Img_Set 3, the proposed model records the highest value (0.6789), outperforming HIS-log Gabor (0.6500) and YCbCr-DWT (0.6151). In Img_Set 4, the proposed model shows an improvement with Q^(AB/F)of 0.6184, surpassing all other methods, including HIS-log Gabor (0.5979). For Img_Set 5, the proposed model leads again with 0.6428, outperforming YCbCr-DWT (0.6253) and HIS-log Gabor (0.6328). In Img_Set 6, the proposed model (0.6225) matches Shearlet (0.6207) and outperforms HIS-log Gabor (0.5016). For Img_Set 7, the proposed model achieves the highest. Q^(AB/F) (0.6916), significantly outperforming all other methods, including YCbCr-DWT (0.6332). In Img_Set 8, the proposed model continues its dominance with a value of 0.6307.

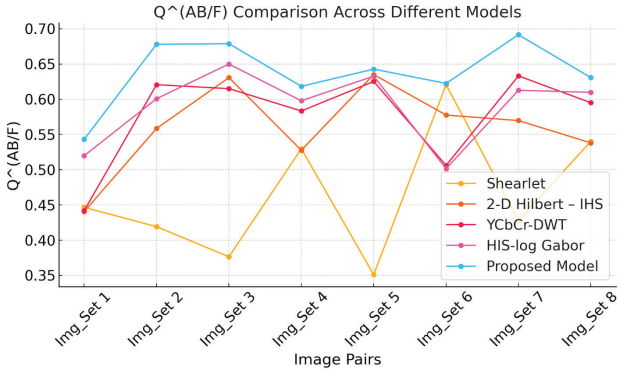

Fig. 13. $Q^{AB/F}$ *comparison.*

CONCLUSION AND FUTURE WORK

I Medical imaging has long been a non-invasive method for diagnosing and treating diseases. Advances in imaging and image processing technologies have led to the development of various medical image modalities. While each modality has a unique characteristic and strength, combining these images can provide a more comprehensive view, enabling medical practitioners to make more accurate diagnoses and plan treatments accordingly. This paper presents a novel medical Image Fusion Model (IFM) aimed to overcome the limitations of the traditional fusion methods. The proposed model integrates FDCT, HVS, and DC-PCNN to fuse MRI and PET images. The MRI images are decomposed using FDCT, while the PET images are decomposed using the HSV color model. The high-frequency (HF) components are fused using DC-PCNN model, and low-frequency (LF) components are fused using a contrast-based weighting method.

The proposed model was compared with other fusion models across various metrics. The experiments used eight image pairs from MRI and PET modalities, sourced from the Harvard Medical School Image Database. The images were grouped into Img_ set 1 to Img_set 8. The results indicate that the proposed model demonstrated competitive performance in all metrics. In Img-Set 2, the proposed model achieved the highest spatial frequency (SF) of 38.79, and in Img_Set 3, it achieved 32.73. For mutual information (MI), the proposed model recorded 3.81 in Img_Set 6. It also achieved the highest image entropy (IE) value of 5.56 in Img_Set 6, the highest Image Quality Index (IQI) of 0.5928 in Img_Set 6, and the highest Margin Information Retention (MIR) value of 0.6916 in Img_Set 7.

However, the dataset used was small (only eight image pairs), and further work is needed to validate the model with a larger dataset and across different imaging modalities.

Future work will focus on expanding the dataset to include a larger number of MRI and PET image pairs, which will improve the robustness and generalizability of the proposed model. Additionally, the model will be tested across other medical imaging modalities to assess its versatility and performance in different diagnostic contexts. Another key direction will be to incorporate deep learning-based fusion methods into the comparison, evaluating how these approaches might enhance the quality of fusion. Ablation studies will also be conducted to justify the individual components of the fusion process, including comparing FDCT with DCT and DWT, as well as evaluating the contributions of DC-PCNN and contrast-based LF fusion. Furthermore, future research will explore new fusion strategies and assess their effectiveness in improving diagnostic outcomes, ensuring the model remains adaptable and effective in a clinical setting.

CONFLICT OF INTEREST

The authors declare that they have no conflict of interest.

DATA AVAILABILITY STATEMENT

The data that support the findings of this study are available from the corresponding author upon reasonable request.

HUMAN PARTICIPANTS

There was no involvement of human patients and participants in the study.

REFERENCES

Abhisheka B, Biswas SK, Purkayastha B (2023). A comprehensive review on breast cancer detection, classification and segmentation using deep learning. Arch Comput Methods Eng 30:5023-52.

Abhisheka B, Biswas SK, Purkayastha B, Das D, Escargueil A (2024). Recent trend in medical imaging modalities and their applications in disease diagnosis: a review. Multimed Tools Appl 83:43035-70.

Amiri E, Rahmanian M, Amiri S, Yazdani Praee H (2021). Medical images fusion using two-stage combined model DWT and DCT. Int Adv Res Eng J 5:344-51.

Arabi H, Saberi Manesh A, Zaidi H (2024). Innovations in dedicated PET instrumentation: from the operating room to specimen imaging. Phys Med Biol 69:11TR03.

Ashwanth B, Swamy KV (2020). Medical image fusion using transform techniques. In: Proc. 2020 5th Int Conf Devices, Circuits and Systems (ICDCS), 2020 Mar 5-6; Coimbatore, India. Piscataway (NJ): IEEE, 303-6.

Bilal A, Imran A, Baig TI, Liu X, Long H, Alzahrani A, Shafiq M (2024a). DeepSVDNet: a deep learning-based approach for detecting and classifying vision-threatening diabetic retinopathy in retinal fundus images. Comput Syst Sci Eng 48:511-28.

Bilal A, Imran A, Liu X, Liu X, Ahmad Z, Shafiq M, El-Sherbeeny AM, Long H (2024b). BC-QNet: a quantum-infused ELM model for breast cancer diagnosis. Comput Biol Med 175:108483.

Bilal A, Liu X, Baig TI, Long H, Shafiq M (2023). EdgeSVDNet: 5G-enabled detection and classification of vision-threatening diabetic retinopathy in retinal fundus images. Electronics 12:4094.

Bilal A, Liu X, Shafiq M, Ahmed Z, Long H (2024c). NIMEQ-SACNet: a novel self-attention precision medicine model for vision-threatening diabetic retinopathy using image data. Comput Biol Med 171:108099.

Chen C-I (2017). Fusion of PET and MR brain images based on IHS and log-Gabor transforms. IEEE Sens J 17:6995-7010.

Eckhorn R, Reitboeck HJ, Arndt M, Dicke P (1989). A neural network for feature linking via synchronous activity: results from cat visual cortex and from simulations. In: Cotterill RMJ, ed. Models of brain function. Cambridge: Cambridge University Press, 255-72.

Furtado FS, Wu MZ, Esfahani SA, Ferrone CR, Blaszkowsky LS, Clark JW, Ryan DP, Goyal L, Franses JW, Wo JY, Hong TS, Qadan M, Tanabe KK, Weekes CD, Cusack JC, Crafa F, Mahmood U, Anderson MA, Mojtahed A, Hahn PF, Caravan P, Kilcoyne A, Vangel M, Striar RM, Rosen BR, Catalano OA (2023). Positron emission tomography/magnetic resonance imaging (PET/MRI) versus the standard of care imaging in the diagnosis of peritoneal carcinomatosis. Ann Surg 277:e893-9.

Haddadpour M, Daneshvar S, Seyedarabi H (2017). PET and MRI image fusion based on combination of 2-D Hilbert transform and IHS method. Biomed J 40:219-25.

Haribabu M, Guruviah V, Yogarajah P (2023). Recent advancements in multimodal medical image fusion techniques for better diagnosis: an overview. Curr Med Imaging 19:673-94.

Islam SMS, Nasim MAA, Hossain I, Ullah DMA, Gupta DKD, Bhuiyan MMH (2023). Introduction of medical imaging modalities. In: Zheng B, Andrei S, Sarker MK, Gupta KD, eds. Data-driven approaches on medical imaging. Cham: Springer, 1-25.

Johnson JL, Padgett ML (1999). PCNN models and applications. IEEE Trans Neural Netw 10:480-98.

Johnson JL, Ranganath H, Kuntimad G, Caulfield H (1998). Pulse-coupled neural networks. In: Omidvar O, Dayhoff JE, eds. Neural networks and pattern recognition. Academic Press, 1-56.

Johnson JL, Ritter D (1993). Observation of periodic waves in a pulse-coupled neural network. Opt Lett 18:1253-5.

Karim S, Tong G, Li J, Qadir A, Farooq U, Yu Y (2023). Current advances and future perspectives of image fusion: a comprehensive review. Inf Fusion 90:185-217.

Li H, Manjunath B, Mitra SK (1995). Multisensor image fusion using the wavelet transform. Graph Models Image Process 57:235-45.

Murtaza G, Shuib L, Abdul Wahab AW, Mujtaba G, Mujtaba G, Nweke HF, Al-garadi MA, Zulfiqar F, Raza G, Azmi NA (2020). Deep learning-based breast cancer classification through medical imaging modalities: state of the art and research challenges. Artif Intell Rev 53:1655-720.

Nobariyan B, Amini N, Daneshvar S, Abbasi A (2018). A novel architecture of medical image fusion based on YCbCr-DWT transform. Int Arab J Inf Technol 15:850-6.

Perez RC, Kim D, Maxwell AWP, Camacho JC (2023). Functional imaging of hypoxia: PET and MRI. Cancers 15:3336.

Preethi S, Aishwarya P (2021). An efficient wavelet-based image fusion for brain tumor detection and segmentation over PET and MRI image. Multimed Tools Appl 80:14789-806.

Rana DH, Degadwala SD (2014). Medical image fusion using combined multi-resolution and multi-scaling transform. Int J Comput Appl 107:26-9.

Ranganath H, Kuntimad G, Johnson JL (1995). Pulse coupled neural networks for image processing. In: Proc. IEEE Southeastcon '95. Visualize the Future, 1995 Mar 26-29; Raleigh, NC. Piscataway (NJ): IEEE, 37-43.

Sayadi M, Ghassemian H, Naimi R (2020). A new composite multimodality image fusion method based on shearlet transform and retina inspired model. In: Proc. 2020 Int Conf Machine Vision and Image Processing (MVIP), 2020 Feb 18-20; Qom, Iran. Piscataway (NJ): IEEE.

Singh P, Bhandari AK (2024). Laplacian and gaussian pyramid based multiscale fusion for nighttime image enhancement. Multimed Tools Appl:1-25.

Singh S, Singh H, Bueno G, Deniz O, Singh S, Monga H, Hrisheekesha PN, Pedraza A (2023). A review of image fusion: methods, applications and performance metrics. Digit Signal Process 137:104020.

Wang Z, Ma Y (2007). Dual-channel PCNN and its application in the field of image fusion. In: Proc. 3rd Int Conf Natural Computation (ICNC 2007), 2007 Aug 24-27; Haikou, China. Los Alamitos (CA): IEEE Computer Society, 755-59.